AGU PUBLICATIONS

Geophysical Research Letters

RESEARCH LETTER

10.1002/2015GL063570

Key Points:

- Major faults are not uniformly distributed and have nonrandom orientations
- Dichotomy between north and south hemispheres in total length of major faults
- Existing global stress models cannot fully account for the faults

Supporting Information:

- Texts S1 and S2, Figures S1–S5, and Table S1

Correspondence to:
T. R. Watters,
watterst@si.edu

Citation:
Watters, T. R., M. M. Selvans, M. E. Banks, S. A. Hauck II, K. J. Becker, and M. S. Robinson (2015), Distribution of large-scale contractional tectonic landforms on Mercury: Implications for the origin of global stresses, *Geophys. Res. Lett.*, *42*, 3755–3763, doi:10.1002/2015GL063570.

Received 27 FEB 2015
Accepted 4 MAY 2015
Accepted article online 7 MAY 2015
Published online 29 MAY 2015

Distribution of large-scale contractional tectonic landforms on Mercury: Implications for the origin of global stresses

Thomas R. Watters[1], Michelle M. Selvans[1], Maria E. Banks[1], Steven A. Hauck II[2], Kris J. Becker[3], and Mark S. Robinson[4]

[1]Center for Earth and Planetary Studies, National Air and Space Museum, Smithsonian Institution, Washington, District of Columbia, USA, [2]Department of Earth, Environmental, and Planetary Sciences, Case Western Reserve University, Cleveland, Ohio, USA, [3]Astrogeology Science Center, United States Geological Survey, Flagstaff, Arizona, USA, [4]School of Earth and Space Exploration, Arizona State University Tempe, Flagstaff, Arizona, USA

Abstract The surface of Mercury is dominated by contractional tectonic landforms that are evidence of global-scale crustal deformation. Using MESSENGER orbital high-incidence angle imaging and topographic data, large-scale lobate thrust fault scarps have been mapped globally. The spatial distribution and areal density of the contractional landforms are not uniform; concentrations occur in longitudinal bands and between the north and south hemispheres. Their orientations are generally north-south at low latitude to midlatitude and east-west at high latitudes. The spatial distribution and distribution of orientations of these large-scale contractional features suggest that planet-wide contraction due to interior cooling cannot be the sole source of global stresses. The nonrandom orientations are best explained by a combination of stresses from global contraction and tidal despinning combined with an equator-to-pole variation in lithospheric thickness, while the nonuniform areal density of the contractional features may indicate the influence of mantle downwelling or heterogeneities in lithospheric strength.

1. Introduction

The first view of the contractional deformation on Mercury was obtained by Mariner 10 during three flybys of the same hemisphere of the planet. Lobate scarps, thrust fault scarps hundreds of kilometers in length, were found to be broadly distributed in the imaged hemisphere [*Strom et al.*, 1975; *Melosh and McKinnon*, 1988; *Watters et al.*, 2004]. Images returned during the three flybys of the MErcury Surface, Space ENvironment, GEochemistry, and Ranging (MESSENGER) spacecraft revealed many more lobate scarps and that they are globally distributed [*Solomon et al.*, 2008; *Watters et al.*, 2009a]. However, the true spatial distribution of the lobate scarps remained poorly defined because the flyby images were of variable spatial resolution and variable lighting geometries that were less than ideal for the global identification and characterization of tectonic landforms. Several MESSENGER orbital imaging campaigns with the Mercury Dual Imaging System (MDIS) wide-angle and narrow-angle cameras [*Hawkins et al.*, 2007] have provided near global monochrome high-incidence angle mosaics along with targeted high-resolution images. These mosaics and images, combined with topography from the Mercury Laser Altimeter (MLA) in the Northern Hemisphere [*Zuber et al.*, 2012] and stereo imaging [*Oberst et al.*, 2010; *Preusker et al.*, 2011], have facilitated the production of comprehensive global maps of the larger scale, most readily discernible lobate scarps and structurally related, though rarer, high-relief ridges. Here we describe the global spatial distribution of these prominent lobate scarps and high-relief ridges. The spatial distribution and pattern of orientations of these landforms are used evaluate models for the origin of global stresses on Mercury.

2. Spatial Distribution and Orientations

Contractional deformation on Mercury is expressed by three, broadly distributed tectonic landforms: lobate scarps, high-relief ridges, and wrinkle ridges. Each of these contractional landforms has a generally distinct morphology, and analogous structures on the other terrestrial planets have been well documented [see *Watters and Schultz*, 2010]. The largest and most widely distributed of these are lobate scarps, linear to

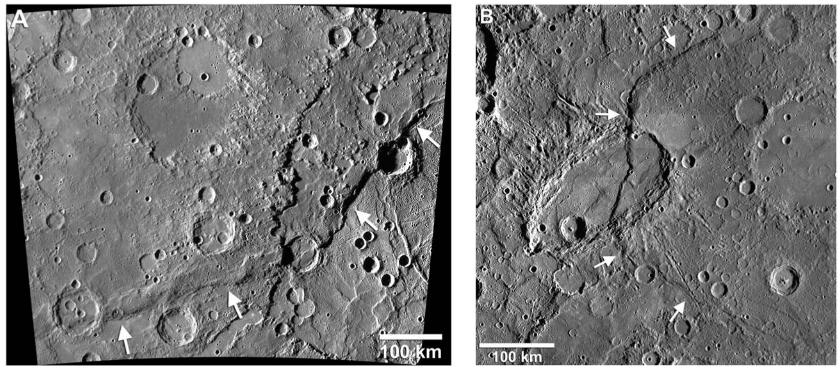

Figure 1. High-incidence angle mosaic of Enterprise Rupes and Beagle Rupes. (a) Enterprise Rupes is the largest lobate scarp found on Mercury. The thrust fault scarp crosscuts the rim and floor of the Rembrandt basin (37°S, 74°E). White arrows show the location of the Enterprise Rupes. (b) Beagle Rupes is a bow-shaped landform and is one the most arcuate lobate scarp found on Mercury. The fault scarp crosscuts the elliptically shaped Sveinsdóttir crater (3°S, 100°E), with a long axis diameter of ~220 km. White arrows show the location of the Beagle Rupes.

arcuate landforms generally asymmetric in cross section with a steeply sloping scarp face and a gently sloping back limb (Figures 1a and 1b) [*Strom et al.*, 1975; *Melosh and McKinnon*, 1988; *Watters et al.*, 1998]. Lobate scarps are recognized by surface-breaking thrust faults that often vertically offset the walls and floors of crosscut impact craters and basins (Figures 1a and 1b) [*Strom et al.*, 1975; *Melosh and McKinnon*, 1988; *Watters et al.*, 1998, 2001, 2009a, 2009b; *Solomon et al.*, 2008], and may be linear to arcuate in plan view. The largest lobate scarp found on Mercury crosscuts the rim and floor of the Rembrandt basin (Figure 1a) [*Watters et al.*, 2009c]. Named Enterprise Rupes, this scarp is nearly 1000 km long and has more than 3 km of relief [*Watters et al.*, 2009c, 2013]. One of the most arcuate scarps revealed by MESSENGER is Beagle Rupes (Figure 1b) [*Solomon et al.*, 2008; *Watters et al.*, 2009a]. The bow-shaped scarp is over 600 km long and crosscuts the elliptically shaped Sveinsdóttir crater. Rarer than lobate scarps, high-relief ridges are more symmetric in cross section (Figures 2a and 2b). High-relief ridges also exhibit horizontal shortening and vertical offsets of the walls and floors of transected impact craters, suggesting that they are also formed by reverse faults [*Watters et al.*, 2001, 2004; *Solomon et al.*, 2008; *Watters and Nimmo*, 2010]. One of the largest high-relief ridges found on Mercury is over 600 km long and transitions into a lobate scarp (Figure 2a) [*Watters et al.*, 2009a]. The existence of such a transition from a high-relief ridge to a lobate scarp is an expression of the close relationship between the two contractional landforms [*Watters et al.*, 2001, 2009a; *Watters and Nimmo*, 2010]. The most morphologically complex contractional landforms are wrinkle ridges, often consisting of a broad, low-relief arch with a narrow superimposed ridge. Wrinkle ridges are interpreted to be formed by a combination of folding and faulting, involving either a single planar or listric thrust fault or a primary thrust fault and a secondary backthrust [*Golombek et al.*, 1991; *Watters*, 1988, 2004; *Schultz*, 2000].

We analyze the most prominent lobate scarps and high-relief ridges, defined here as those with lengths $>$50 km and with more than several hundred meters of relief. Faults of this length scale are the minimum assumed to penetrate to depths of 30–60 km, the likely thickness of the brittle zone at the time of thrust faulting [*Watters et al.*, 2002; *Nimmo and Watters*, 2004; *Zuber et al.*, 2010]. Thus, this population of faults provides a crucial avenue to assess the distribution and orientation of dominant stresses in Mercury's lithosphere. These large faults deform heavily cratered terrain and intercrater plains emplaced before the end of late heavy bombardment (LHB), as well as younger, Calorian-aged smooth plains volcanic deposits [*Watters et al.*, 2004, 2009a; *Watters and Nimmo*, 2010]. Wrinkle ridges are not included because they are confined to younger smooth plains with more shallowly rooted thrust faults. These landforms are expected to result from a combination of load-induced flexure and subsidence with only some contribution of stresses from global sources [*Watters et al.*, 2009a], and their orientations are often strongly influenced by the boundary conditions of the smooth plains they deform [*Watters and Nimmo*, 2010]. The approach to mapping the tectonic landforms in this study differs from that taken by *Byrne et al.* [2014]. They grouped lobate scarps, high-relief ridges, wrinkle ridges, and many other positive relief landforms of

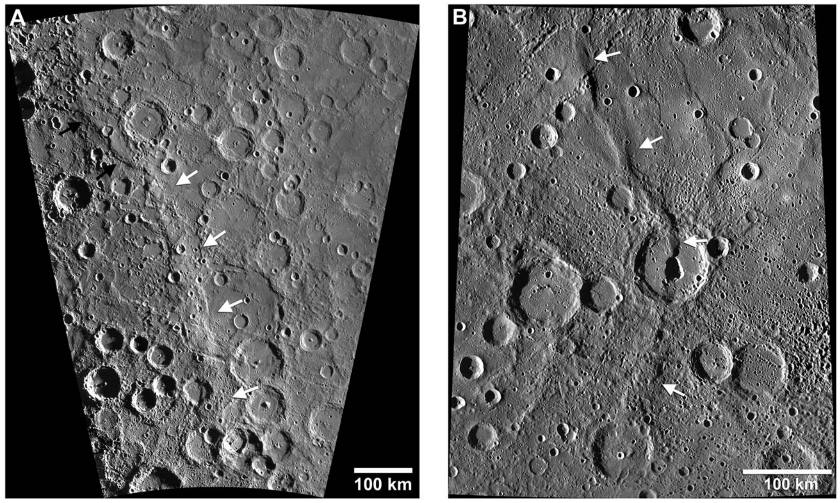

Figure 2. High-incidence angle image mosaic of high-relief ridges. (a) This remarkably linear high-relief ridge (58°S, 105°E) is one of the largest found on Mercury. At its northern end, the ridge transition into a lobate scarp. White arrows show the location of the high-relief ridge, and black arrows show the location of the lobate scarp. (b) Antoniadi Dorsa is a high-relief ridge that crosscuts an ~85 km diameter impact crater (27°N, 30°W). White arrows show the location of the high-relief ridge.

all scales together as shortening structures classified by the terrain type they deform (i.e., cratered plains structures or smooth plains structures).

A fundamental observation that can be made from the spatial distribution and areal density of the largest contractional landforms is that they are not uniformly distributed on the surface of Mercury (Figure 3a). Mapping using global high-incidence angle mosaics generated with opposite solar azimuth directions obtained largely during the third and fourth solar day of MESSENGER's orbital mission shows areas with distinctly fewer lobate scarps, as noted in earlier studies [*Watters et al*., 2004, 2009a]. The large-scale structures form a minimum of two pronounced concentrations that occur in broad longitudinal bands (centered approximately at −30° and 110°) and a less pronounced third band (at approximately −90°) separated by regions where there are distinctly fewer such tectonic features (Figures 3a and 3b). These bands, also expressed by the cumulative length of the structures as a function of longitude (Figure 3c), do not generally correspond to zones with the highest incidence angles ($>$ ~85°) images and are thus not likely an artifact of lighting geometry (see supporting information, Figure S1). A plot of the weighted means of orientations scaled by total length confirms that there are areas with fewer large-scale contractional landforms (Figure 3b). Within the longitudinal bands, the lobate scarps exhibit a range of orientations. At low to midlatitudes (roughly ±60°), orientations are generally N-S. However, some generally E-W oriented lobate scarps are found at low to midlatitudes, indicating that the dominant N-S orientation is not the result of local illumination direction bias (see supporting information). At southern high latitudes, poleward of 60°S, the dominant orientation is roughly E-W. Scarps and ridges in the southern high latitudes appear to form a latitudinal band (Figures 3a and 3b).

Another distinctive feature of the global distribution of these structures is the difference in number and scale of lobate scarps and high-relief ridges between the northern and southern hemispheres (Figures 3a and 3b). The greatest concentrations of large-scale lobate scarps are located in the southern hemisphere. The total length of mapped large-scale lobate scarps and high-relief ridges in the southern hemisphere (~33,000 km) is more than a factor of two greater than the total mapped length in the northern hemisphere (~14,000 km). The distribution of the largest fault scarps also contributes to the difference in total length between the hemispheres, with nearly three times more faults $>$100 km in length occurring in the southern hemisphere. This dichotomy between the hemispheres is strongly correlated with the distribution of smooth plains (Figures 3a and 3b) (see supporting information). Large expanses of intercrater plains in the northern hemisphere where lobate scarps and high-relief ridges are nearly absent (Figures 3a and 3b) suggest that the distribution of smooth plains alone does

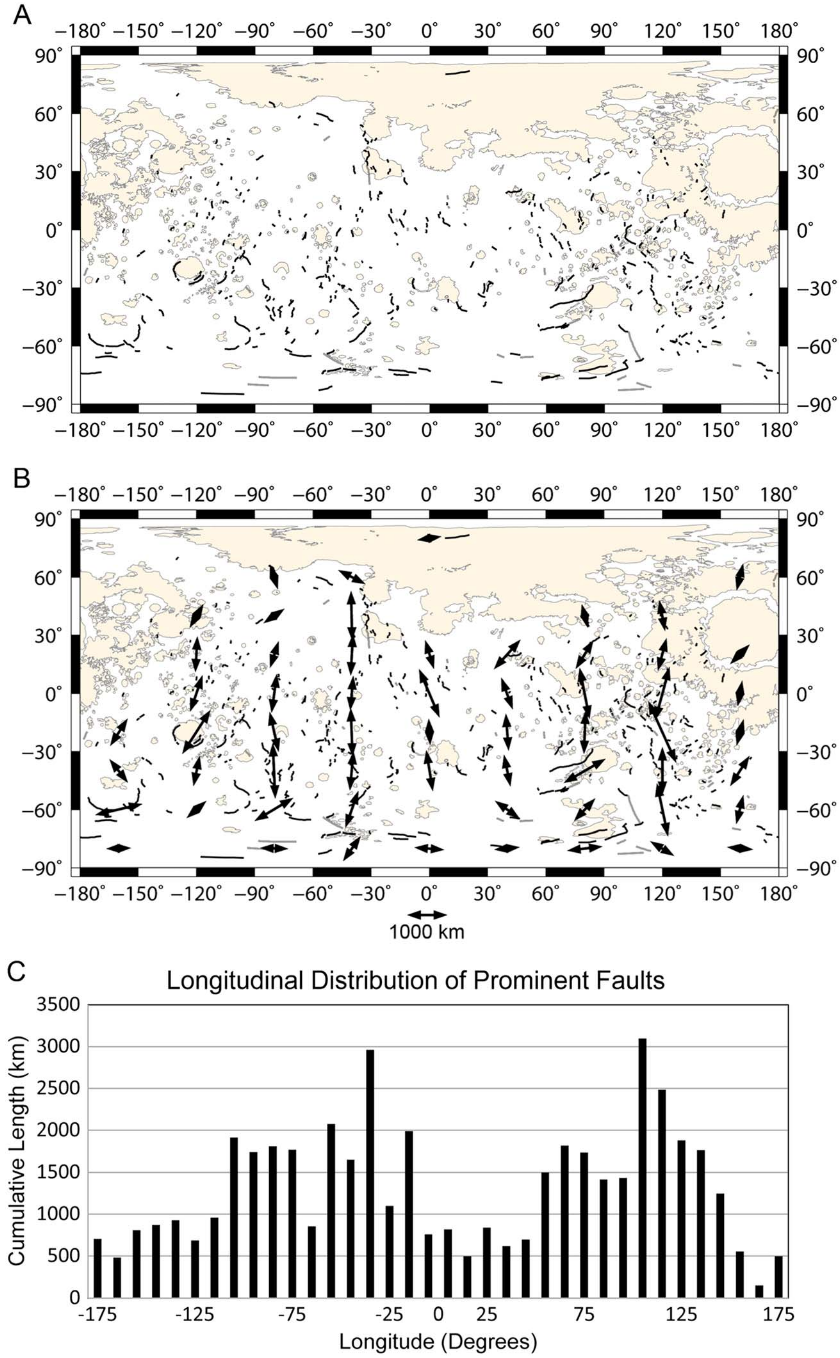

Figure 3. Map of prominent contractional tectonic landforms. (a) Global map of lobate scarps (black) and high-relief ridges (gray) >50 km in length on Mercury. The contractional features are distributed in broad, longitudinal bands. (b) Plot of weighted means of orientations of the large-scale lobate scarps and high-relief ridges. Digitized segments are sampled in areas with dimensions of 40° × 20° (longitude and latitude) and orientation vectors are scaled by the total length of the structures within the sampling area. Sampled area with a total length of mapped structures <100 km is not shown. Smooth plains units [*Denevi et al.*, 2013] are shown in tan. (c) Plot of cumulative length of large-scale lobate scarps and high-relief ridges as a function of longitude. Two pronounced concentrations occur in broad longitudinal bands centered roughly at –30° and 110°, with a third less pronounced concentration at –90°. The lengths of the structures are sampled in 10° bins.

not account for the dichotomy. However, other factors such as major crustal or lithospheric heterogeneities may contribute to the difference.

3. Models for Global Stresses

Many models have been proposed for the origin of the stresses that resulted in the distribution of lobate scarps first observed in the hemisphere imaged by Mariner 10. These lithospheric stress models involve global contraction accompanying interior cooling, tidal despinning, reorientation of the poles, or a combination of some or all of these stresses [*Strom et al*., 1975; *Solomon*, 1979; *Pechmann and Melosh*, 1979; *Melosh and McKinnon*, 1988; *Schubert et al*., 1988; *Hauck et al*., 2004; *Dombard and Hauck*, 2008; *Matsuyama and Nimmo*, 2009; *Beuthe*, 2010]. Each model predicts details about the type, spatial distribution, and orientations of the faults. The most widely accepted model is global contraction which, absent other influences, would result in global, horizontally isotropic compressional stress and a more or less uniformly distributed population of randomly oriented lobate scarps [e.g., *Watters et al*., 2004, 2009a] with the onset of contraction before the end of LHB [*Solomon*, 1979; *Schubert et al*., 1988; *Hauck et al*., 2004; *Dombard and Hauck*, 2008]. The spatial distribution and preferred orientations of the prominent lobate scarps (Figures 3a and 3b) are not consistent with uniform global contraction as the sole source of stress. Tidal despinning, the slowing of an initial rapid rate of rotation, predicts predominantly N-S trending faults near the equator [*Melosh and McKinnon*, 1988]. The despinning model also predicts strike-slip faults in the midlatitudes and E-W normal faults at high latitudes. The predicted faults do not agree well with the distribution of lobate scarps and high-relief ridges. While N-S trending faults are common in the equatorial region, they are also found at midlatitudes where strike-slip faults are predicted. At high latitudes, E-W thrust faults not normal faults are observed. The equatorial N-S thrust faults suggest either a relatively thick lithosphere at the time of faulting or the addition of isotropic compressional stress from global contraction [*Melosh and McKinnon*, 1988; *Watters and Nimmo*, 2010]. The combination of despinning and global contraction has the advantage of increasing the latitudinal range of N-S oriented thrust faults [*Pechmann and Melosh*, 1979; *Melosh and McKinnon*, 1988; *Dombard and Hauck*, 2008; *Beuthe*, 2010; *Klimczak et al*., 2015].

Dombard and Hauck [2008] modeled stresses from despinning together with global contraction of at least 3–5.5 km prior to the end of LHB (~4 Ga). The resulting stress would generate a global population of N-S oriented thrust faults. Their model predicts comparable amounts of post-LHB radial contraction, in excess of the 1–2 km estimated from Mariner 10 and MESSENGER flyby-based surveys [*Strom et al*., 1975; *Watters et al*., 1998, 2009a; *Watters and Nimmo*, 2010], that suggested a significant component of unaccounted for strain. However, recent studies using more inclusive criteria of mapping contractional features and that include wrinkle ridges have yielded estimates of post-LHB radial contraction of up to ~4 [*Di Achille et al*., 2012] to 7 km [*Byrne et al*., 2014]. Larger amounts of post-LHB contraction allow a greater range of less restricted initial conditions for thermal models and more consistent with predicted amounts of accumulated contraction [*Solomon*, 1977; *Dombard and Hauck*, 2008].

Although the model of *Dombard and Hauck* [2008] predicts the broader areal distribution of N-S oriented lobate scarps at low to midlatitudes, it does not account for E-W oriented thrust faults at high latitudes. *Beuthe* [2010] suggests that a combination of despinning and global contraction could generate a high-latitude zone of E-W thrust faults if equatorial thinning of the lithosphere is extended poleward, such as might be expected with Mercury's large latitudinal variation surface temperatures [*Williams et al*., 2011]. The *Beuthe* [2010] model with a latitudinal transition in lithospheric thickness predicts N-S oriented thrust faults at latitudes of ±60° and E-W oriented faults at latitudes greater than ±60° [see *Beuthe*, 2010, Figure 8], in reasonable agreement with the observed distribution of orientations of the mapped faults (Figure 4a). Furthermore, for greater values of expansion of poleward thinning of the lithosphere, the transition between N-S and E-S thrust faults at about ±60° corresponds to a ratio of contraction to despinning stresses of ~1 [see *Beuthe*, 2010, Figure 9].

Taking the approach of *Melosh and McKinnon* [1988] to model latitudinal variations in stress from a combination of despinning and global contraction, *Klimczak et al*. [2015] propose an alternative to equatorial thinning to extend the zone of N-S oriented thrust faults. They suggest Mercury's pervasive fractured brittle lithosphere will be significantly weaker than previous thought (deformation modulus

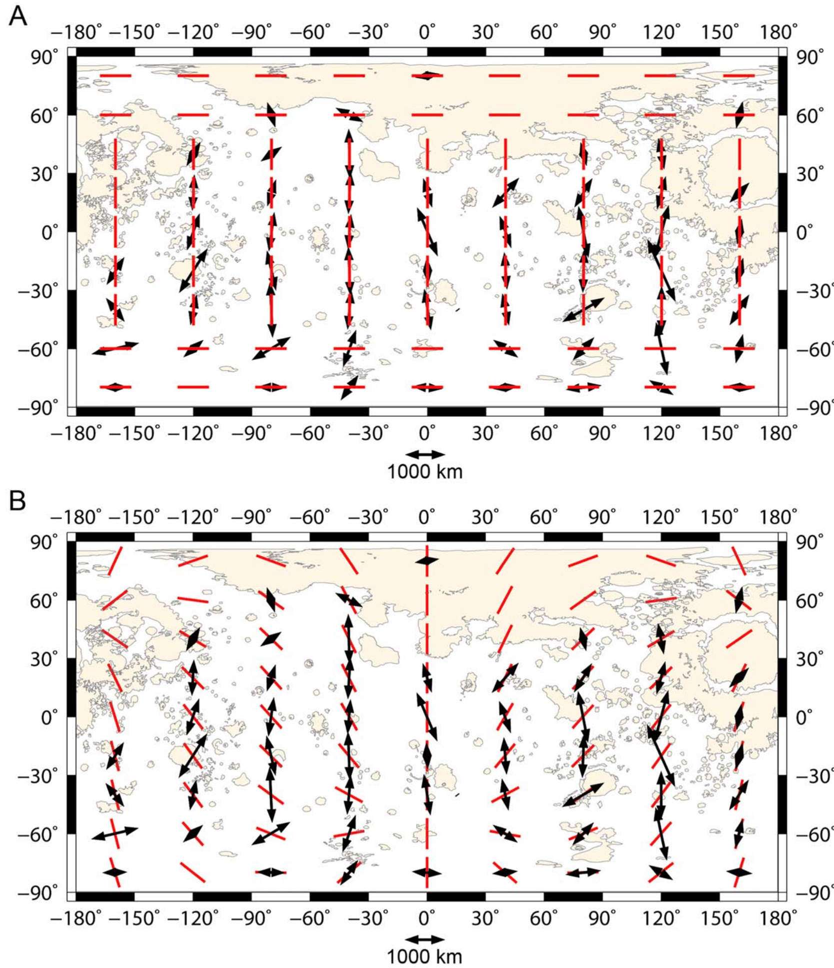

Figure 4. Models for global stresses on Mercury. (a) Predicted faults due to a combination of tidal despinning and global contraction. The predicted distribution of N-S and E-W oriented thrust faults (red lines) results from the combination of tidal despinning and global contraction combined with an equator-to-pole variation in lithosphere thickness [*Beuthe*, 2010]. (b) Predicted faults due to despinning, equatorward reorientation of the poles, and global contraction. The orientation of the predicted thrust faults (red lines) is radial to locations of the initial rotational poles [*Matsuyama and Nimmo*, 2009, model C]. Orientation vectors of the lobate scarp and high-relief ridge are shown for comparison (see Figure 3b).

E^* ~7.5 to 50 GPa) based on the use of an empirical rock mass failure criteria developed to assess the strength of shallow-depth rock masses. However, *Klimczak et al*. [2015] predict thrust faults with no preferred orientations at high latitudes. This is not in agreement with the observed distribution of orientations of the fault scarps (Figures 3a and 3b).

Matsuyama and Nimmo [2009] modeled despinning and reorientation of a remnant bulge with a large gravity anomaly associated with the Caloris basin inducing equatorward reorientation of the poles. MESSENGER has confirmed a large free-air gravity anomaly (mascon) associated with the Caloris basin [*Smith et al*., 2012]. The faults predicted from the reorientation and despinning models of *Matsuyama and Nimmo* [2009] that include radial contraction are generally not a good fit to the observed distribution and orientations of the largest contractional faults (Figure 4b), especially at the locations of the initial rotational poles [see *Matsuyama and Nimmo*, 2009, Figure 6].

While the dominant orientations can be explained by a combination of stresses from global contraction and tidal despinning, such a model does not account for the nonuniform spatial distribution of the faults. Their nonuniform distribution suggests other mechanisms contribute to the localization of the faults. One mechanism that has been proposed is mantle convection [*King*, 2008]. Three-dimensional models of mantle convection predict patterns of additional compressional stresses along zones of mantle downwelling that might act to enhance localization of N-S oriented contractional faults at low latitudes with generally E-W contractional faults in the polar regions [*King*, 2008]. This pattern of faults is broadly consistent with the orientations of prominent lobate scarps. However, reductions in estimates for the thickness of Mercury's mantle reduce the expected vigor and longevity of convection [*Smith et al*., 2012; *Hauck et al*., 2013; *Tosi et al*., 2013] capable of providing such a source of additional localizing stresses. Furthermore, recent models [*Michel et al*., 2013; *Tosi et al*., 2013] suggest that the maximum size of a convective cell is generally on the scale of the thickness of the convecting layer; and thus, no large-scale linear patterns at the scale observed in MESSENGER data (Figure 3) are predicted [see *Tosi et al*., 2013, Figure 5].

Alternatively, localized mantle downwelling has been suggested to concentrate the lobate scarps [*Watters et al*., 2004]. Intraplate mantle downwelling on Earth has been invoked as a mechanism to thicken crust and localize compressional stresses in the lithosphere [*Neil and Houseman*, 1999]. An analysis of the locations of large-scale faults in the northern hemisphere and crustal thickness, modeled using dual inversion of topography and gravity data [*James et al*., 2015], indicates faults are preferentially concentrated in regions of greater crustal thickness and in areas with negative mantle dynamic pressure as might be expected if faults were localized by zones of mantle downwelling [*Selvans et al*., 2014]. Thus, downward mantle flow may contribute to the localization and concentration of the faults.

Another explanation for the nonuniform density of tectonic landforms is heterogeneities in the strength of the lithosphere. One possibility is that differences in lithospheric strength could be due to variations in solar insolation. *Williams et al*. [2011] predict that such strength difference would result in differences in the distribution and orientation of faulting between the hot (0° and ±180° longitude) and warm (±90° longitude) poles of Mercury's surface. However, the areal density of large faults is significantly lower at the hot poles (Figure 3). This is the case even if the faults in the northern hemisphere where smooth plains dominate are ignored. Also, no discernible variations in the orientations of the faults are found between the longitudes of the equatorial hot and warm poles (Figure 3).

4. Summary and Conclusions

Global contraction is the most commonly cited model for the stresses that formed the population of lobate scarps on Mercury. The near absence of extensional tectonic landforms outside of impact basins and ghost basins and craters [see *Watters et al*., 2012] is compelling evidence of a lithosphere in a general state of compression since the end of LHB. However, it is clear that global contraction alone cannot account for the spatial distribution and orientations of the large-scale faults. The models examined that best account for the contractional landforms are a combination of global contraction and tidal despinning [*Dombard and Hauck*, 2008; *Beuthe*, 2010; *Klimczak et al*., 2015]. Extending equatorial thinning, consistent with the large latitudinal variation in surface temperatures [e.g., *Williams et al*., 2011], of the lithosphere poleward as suggested by *Beuthe* [2010] successfully predicts the distribution of both N-S and E-W oriented thrust faults and avoids the need for an unusually weak brittle lithosphere invoked by *Klimczak et al*. [2015]. The transition between N-S and E-S thrust faults at about ±60° suggests roughly equal contribution of stress from global contraction and tidal despinning [see *Beuthe*, 2010]. Timing is critical for the despinning-contraction models since stresses related to tidal despinning likely peak prior to the end of LHB [*Melosh and McKinnon*, 1988]. Reactivation of pre-LHB faults, both contractional and extensional, may be necessary to account for the orientations of large-scale lobate scarps [*Dombard and Hauck*, 2008; *Watters and Nimmo*, 2010]. A combination of global contraction and tidal despinning, however, does not account for the nonuniform areal density of the contractional landforms. Mantle convection has been suggested as a mechanism to concentrate the faults [*King*, 2008]; however, convection models that include the revised interior structure models for Mercury [*Smith et al*., 2012; *Hauck et al*., 2013; *Michel et al*., 2013; *Tosi et al*., 2013] do not predict convection cells with spatial scales comparable to the observed fault scarp distribution. The correlation between the areal distribution of faults and regions of greater crustal thickness suggests that mantle flow in areas of downwelling [*Watters et al*., 2004; *Selvans et al*., 2014] could contribute to the localization of the large-scale faults. Thus, no single or combination of previously proposed global stress models can account for both the distribution and orientations of Mercury's array of major contractional faults. Other processes or conditions such as mantle flow or heterogeneities in lithospheric strength must be sought.

Acknowledgments
We thank W.B. McKinnon and an anonymous reviewer for helpful comments that greatly improved the manuscript. We also thank S.C. Solomon, P.K. Byrne, and C. Klimczak for helpful suggestion on an early manuscript. We are grateful to the MESSENGER engineers and technical support personnel at Johns Hopkins University Applied Physics Laboratory. This work is also supported by NASA grant NNX07AR60G. Data used to produce the results of this paper can be obtained upon request from the first author.

The Editor thanks William NcKinnon and an anonymous reviewer for their assistance in evaluating this paper.

References

Beuthe, M. (2010), East–west faults due to planetary contraction, *Icarus*, *209*, 795–817.
Byrne, P. K., C. Klimczak, A. M. C. Sengor, S. C. Solomon, T. R. Watters, and S. A. Hauck II (2014), Mercury: Global tectonics on a contracting planet, *Nat. Geosci.*, *7*, 301–307.
Denevi, B. W., et al. (2013), The distribution and origin of smooth plains on Mercury, *J. Geophys. Res. Planets*, *118*, 891–907, doi:10.1002/jgre.20075.
Di Achille, G., C. Popa, M. Massironi, E. Mazzotta Epifani, M. Zusi, G. Cremonese, and P. Palumbo (2012), Mercury's radius change estimates revisited using MESSENGER data, *Icarus*, *221*, 456–460.
Dombard, A. J., and S. A. Hauck II (2008), Despinning plus global contraction and the orientation of lobate scarps on Mercury, *Icarus*, *198*, 274–276.
Golombek, M. P., J. B. Plescia, and B. J. Franklin (1991), Faulting and folding in the formation of planetary wrinkle ridges, *Proc. Lunar Planet. Sci.*, *21*, 679–693.
Hauck, S. A., II, A. J. Dombard, R. J. Phillips, and S. C. Solomon (2004), Internal and tectonic evolution of Mercury, *Earth Planet. Sci. Lett.*, *222*, 713–728.
Hauck, S. A., II et al. (2013), The curious case of Mercury's internal structure, *J. Geophys. Res. Planets*, *118*, 1204–1220, doi:10.1002/jgre.20091.
Hawkins, S. E., III et al. (2007), The Mercury dual imaging system on the MESSENGER spacecraft, *Space Sci. Rev.*, *131*, 247–338, doi:10.1007/s11214-007-9266-3.
James, P. B., M. T. Zuber, R. J. Phillips, and S. C. Solomon (2015), Support of long-wavelength topography on Mercury inferred from MESSENGER measurements of gravity and topography, *J. Geophys. Res. Planets*, *120*, 287–310, doi:10.1002/2014JE004713.
King, S. D. (2008), Pattern of lobate scarps on Mercury's surface reproduced by a model of mantle convection, *Nat. Geosci.*, *1*, 229–232.
Klimczak, C., P. K. Byrne, and S. C. Solomon (2015), A rock-mechanical assessment of Mercury's global tectonic fabric, *Earth Planet. Sci. Lett.*, *416*, 82–90.
Matsuyama, I., and F. Nimmo (2009), Gravity and tectonic patterns of Mercury: Effect of tidal deformation, spin-orbit resonance, nonzero eccentricity, despinning, and reorientation, *J. Geophys. Res.*, *114*, E01010, doi:10.1029/2008JE003252.
Melosh, H. J., and W. B. McKinnon (1988), The tectonics of Mercury, in *Mercury*, edited by F. Vilas, C. R. Chapman, and M. S. Matthews, pp. 374–400, Univ. of Ariz. Press, Tucson.
Michel, N. C., S. A. Hauck II, S. C. Solomon, R. J. Phillips, J. H. Roberts, and M. T. Zuber (2013), Thermal evolution of Mercury as constrained by MESSENGER observations, *J. Geophys. Res. Planets*, *118*, 1033–1044, doi:10.1002/jgre.20049.
Neil, E. A., and G. A. Houseman (1999), Rayleigh-Taylor instability of the upper mantle and its role in intraplate orogeny, *Geophys. J. Int.*, *138*, 89–107.
Nimmo, F., and T. R. Watters (2004), Depth of faulting on Mercury: Implications for heat flux and crustal and effective elastic thickness, *Geophys. Res. Lett.*, *31*, L02701, doi:10.1029/2003GL018847.
Oberst, J., F. Preusker, R. J. Phillips, T. R. Watters, J. W. Head, M. T. Zuber, and S. C. Solomon (2010), The morphology of Mercury's Caloris basin as seen in MESSENGER stereo topographic models, *Icarus*, *209*, 230–238.
Pechmann, J. B., and H. J. Melosh (1979), Global fracture patterns of a despun planet application to Mercury, *Icarus*, *38*, 243–250.
Preusker, F., J. Oberst, J. W. Head, T. R. Watters, M. S. Robinson, M. T. Zuber, and S. C. Solomon (2011), Stereo topographic models of Mercury after three MESSENGER flybys, *Planet. Space Sci.*, *59*, 1910–1917.
Schubert, G., M. N. Ross, D. J. Stevenson, and T. Spohn (1988), Mercury's thermal history and the generation of its magnetic field, in *Mercury*, edited by F. Vilas, C. R. Chapman, and M. S. Matthews, Univ. of Ariz. Press, Tucson.
Schultz, R. A. (2000), Localization of bedding-plane slip and backthrust faults above blind thrust faults: Keys to wrinkle ridge structure, *J. Geophys. Res.*, *105*, 12,035–12,052, doi:10.1029/1999JE001212.
Selvans, M. M., T. R. Watters, P. B. James, and S. C. Solomon (2014), Statistical analysis of the distribution of tectonic features and crustal thickness in the northern hemisphere of Mercury, *Lunar Planet. Sci.*, *45*, Abstract 1442.
Smith, D. E., et al. (2012), Gravity field and internal structure of Mercury from MESSENGER, *Science*, *336*, 212–216.
Solomon, S. C. (1977), The relationship between crustal tectonics and internal evolution in the Moon and Mercury, *Phys. Earth Planet. Inter.*, *15*, 135–145.
Solomon, S. C. (1979), Formation, history and energetics of cores in the terrestrial planets, *Phys. Earth Planet. Inter.*, *19*, 168–182.
Solomon, S. C., et al. (2008), Return to Mercury: A global perspective on MESSENGER's first Mercury flyby, *Science*, *321*, 59–62.
Strom, R. G., N. J. Trask, and J. E. Guest (1975), Tectonism and volcanism on Mercury, *J. Geophys. Res.*, *80*, 2478–2507, doi:10.1029/JB080i017p02478.
Tosi, N., M. Grott, A.-C. Plesa, and D. Breuer (2013), Thermochemical evolution of Mercury's interior, *J. Geophys. Res. Planets*, *118*, 2474–2487, doi:10.1002/jgre.20168.
Watters, T. R. (1988), Wrinkle ridge assemblages on the terrestrial planets, *J. Geophys. Res.*, *93*, 10,236–10,254, doi:10.1029/JB093iB09p10236.
Watters, T. R. (2004), Elastic dislocation modeling of wrinkle ridges on Mars, *Icarus*, *171*, 284–294.
Watters, T. R., and F. Nimmo (2010), The tectonics of Mercury, in *Planetary Tectonics*, edited by T. R. Watters and R. A. Schultz, pp. 15–80, Cambridge Univ. Press, Cambridge.
Watters, T. R., and R. A. Schultz (Eds.) (2010), *Planetary Tectonics*, pp. 530, Cambridge Univ. Press, Cambridge.
Watters, T. R., M. S. Robinson, and A. C. Cook (1998), Topography of lobate scarps on Mercury: New constraints on the planet's contraction, *Geology*, *26*, 991–994.
Watters, T. R., M. S. Robinson, and A. C. Cook (2001), Large-scale lobate scarps in the southern hemisphere of Mercury, *Planet. Space Sci.*, *49*, 1523–1530.
Watters, T. R., R. A. Schultz, M. S. Robinson, and A. C. Cook (2002), The mechanical and thermal structure of Mercury's early lithosphere, *Geophys. Res. Letts.*, *29*(11), 1542, doi:10.1029/2001GL014308.
Watters, T. R., M. S. Robinson, C. R. Bina, and P. D. Spudis (2004), Thrust faults and the global contraction Mercury, *Geophys. Res. Lett.*, *31*, L04701, doi:10.1029/2003GL019171.
Watters, T. R., S. C. Solomon, M. S. Robinson, J. W. Head, S. L. André, S. A. Hauck II, and S. L. Murchie (2009a), The tectonics of Mercury: The view after MESSENGER's first flyby, *Earth Planet. Sci. Lett.*, *285*, 283–296, doi:10.1016/j.epsl.2009.01.025.
Watters, T. R., S. L. Murchie, M. S. Robinson, S. C. Solomon, B. W. Denevi, S. L. André, and J. W. Head (2009b), Emplacement and tectonic deformation of smooth plains in the Caloris basin, Mercury, *Earth Planet. Sci. Lett.*, *285*, 309–319, doi:10.1016/j.epsl.2009.03.040.
Watters, T. R., J. W. Head, S. C. Solomon, M. S. Robinson, C. R. Chapman, B. W. Denevi, C. I. Fassett, S. L. Murchie, and R. G. Strom (2009c), Evolution of the rembrandt impact basin on Mercury, *Science*, *324*, 618–621.

Watters, T. R., S. C. Solomon, C. Klimczak, A. M. Freed, J. W. Head, C. M. Ernst, D. M. Blair, T. A. Goudge, and P. K. Byrne (2012), Extension and contraction within volcanically buried impact craters and basins on Mercury, *Geology*, *40*, 1123–1126.

Watters, T. R., S. C. Solomon, J. Oberst, F. Preusker, S. A. Hauck II, and M. T. Zuber (2013), The rembrandt trough: Evidence of lithospheric folding on Mercury?, *Lunar Planet. Sci.*, *44*, Abstract 2673.

Williams, J.-P., J. Ruiz, M. A. Rosenburg, O. Aharonson, and R. J. Phillips (2011), Insolation driven variations of Mercury's lithospheric strength, *J. Geophys. Res.*, *116*, E01008, doi:10.1029/2010JE003655.

Zuber, M. T., et al. (2010), Accommodation of lithospheric shortening on Mercury from altimetric profiles of ridges and lobate scarps measured during MESSENGER flybys 1 and 2, *Icarus*, *209*, 247–255.

Zuber, M. T., et al. (2012), Topography of the northern hemisphere of Mercury from MESSENGER laser altimetry, *Science*, *336*, 217–220.